

RESEARCH LETTER

10.1002/2017GL075501

Key Points:

- We relate earthquake rupture threshold to physical parameters
- We estimate the variation of the rupture threshold along an actual subduction fault
- We relate estimates of rupture threshold variations to earthquake magnitude

Supporting Information:

- Supporting Information S1

Correspondence to:

Q. Bletery,  
qbletery@uoregon.edu

Citation:

Bletery, Q., Thomas, A. M., Rempel, A. W., & Hardebeck, J. L. (2017), Imaging shear strength along subduction faults. *Geophysical Research Letters*, 44. <https://doi.org/10.1002/2017GL075501>

Received 1 SEP 2017

Accepted 22 OCT 2017

Accepted article online 26 OCT 2017

Imaging Shear Strength Along Subduction Faults

Quentin Bletery<sup>1</sup>, Amanda M. Thomas<sup>1</sup>, Alan W. Rempel<sup>1</sup>, and Jeanne L. Hardebeck<sup>2</sup>

<sup>1</sup>Department of Earth Science, University of Oregon, Eugene, OR, USA, <sup>2</sup>U.S. Geological Survey, Menlo Park, CA, USA

**Abstract** Subduction faults accumulate stress during long periods of time and release this stress suddenly, during earthquakes, when it reaches a threshold. This threshold, the shear strength, controls the occurrence and magnitude of earthquakes. We consider a 3-D model to derive an analytical expression for how the shear strength depends on the fault geometry, the convergence obliquity, frictional properties, and the stress field orientation. We then use estimates of these different parameters in Japan to infer the distribution of shear strength along a subduction fault. We show that the 2011  $M_w$ 9.0 Tohoku earthquake ruptured a fault portion characterized by unusually small variations in static shear strength. This observation is consistent with the hypothesis that large earthquakes preferentially rupture regions with relatively homogeneous shear strength. With increasing constraints on the different parameters at play, our approach could, in the future, help identify favorable locations for large earthquakes.

**Plain Language Summary** Subduction faults accumulate stress during hundreds of years until this stress reaches a threshold. When this threshold is reached, an earthquake occurs. We derive an expression of the rupture threshold depending on different physical parameters, which vary along subduction faults. We then use estimates of the spacial variations of these different parameters in Japan to infer the distribution of the rupture threshold along the Japanese subduction faults. Our results suggest that very large earthquakes, such as the 2011  $M_w$ 9.0 Tohoku earthquake, occur on fault portions of particularly homogeneous rupture thresholds. Our interpretation is that the rupture threshold is more likely to be reached simultaneously on broad fault portions if it does not vary much from one point of the fault to another. Imaging spatial variations of the rupture threshold along large faults may then reveal the location of possible future large earthquakes.

1. Introduction

Earthquakes are the result of relative motion between elastic blocks that is accommodated by slip on active faults. On convergent margins, during prolonged time periods, the contacts between crustal rocks are strong enough to prevent significant slip in the first 40–70 km beneath Earth’s surface. As a result, stress gradually accumulates along these “locked” portions of subduction faults. The accumulated stress is ultimately released when it reaches a threshold that overcomes the shear strength along a fault segment of sufficient extent for an earthquake to nucleate. Once initiated, an earthquake can propagate as long as the dynamic stress perturbation  $\delta\tau$  inherited from earlier phases of the rupture is larger than the difference between the local shear strength  $\tau^c$ —defined as the critical shear stress required to slip at a given location—and the background shear stress  $\tau$ , so that

$$\delta\tau \geq \tau^c - \tau. \tag{1}$$

We see from equation (1) that rupture propagation past any given point is favored by large dynamic stress perturbations  $\delta\tau$  and/or small values of  $\tau^c - \tau$ . Large  $\delta\tau$  is expected from the sudden release of large stress concentrations that were able to build up in regions where the local shear strength  $\tau^c$  was higher than that of surrounding fault segments. On the other hand, high  $\tau^c$  fault segments also produce barriers to rupture propagation by making  $\tau^c - \tau$  larger than in the surroundings so that it can potentially exceed  $\delta\tau$ . Unfortunately, despite this established conceptual understanding, few detailed constraints are available to quantify the terms in equation (1), particularly over the short length scales known to govern earthquake nucleation (e.g., Dieterich, 1981; Li & Rice, 1983; Rice, 1983). Nevertheless, the observation that the largest earthquakes can only occur when equation (1) is satisfied over large areas suggests that a viable strategy for identifying those regions most prone to hosting such events might be based on an approximate analysis

of the mechanical conditions over long wavelengths. Fortunately, the available data on plate geometries, convergence directions, and stress field orientations make it possible to estimate subduction shear strengths  $\tau^c$  and their variations over length scales relevant to mega-earthquake propagation ( $\geq 100$  km). Accordingly, here we pursue the hypothesis that insights on key features of fault behavior—in particular on the maximum earthquake magnitude—may be inferred from the distribution of shear strength.

In an earlier paper we presented a simplified 2-D formulation, assuming hydrostatic pore pressure and neglecting cohesion, of the shear strength as a function of the friction coefficient  $\mu$ , bulk densities of the crust  $\rho$  and water  $\rho_w$ , depth  $h$ , dip angle  $\theta$ , and the angle  $\psi$  between the maximum principal component of stress and the horizontal (Bletery et al., 2016)

$$\tau^c = \frac{gh\mu(\rho - \rho_w)(\sin 2\theta + \tan 2\psi \cos 2\theta)}{\sin 2\theta - \mu(1 - \cos 2\theta) + \tan 2\psi(\cos 2\theta - \mu \sin 2\theta)}. \quad (2)$$

Here we derive a similar expression for the shear strength on any point of a subduction fault in a more general 3-D case that takes into account the obliquity of plate convergence. Our expression for  $\tau^c$  (equation (11)) depends on geometrical ( $h, \theta$ ) and constitutive ( $\mu$ ) parameters, in addition to other factors needed to describe the local state. After outlining our model formulation, we illustrate its implications by evaluating  $\tau^c$  and its spatial variations along the Japanese subduction faults for which the controlling parameters are best constrained. We ultimately show that the 2011  $M_w$ 9.0 Tohoku-Oki earthquake ruptured an area of particularly low shear strength gradient, supporting the idea that shear strength is more likely to be exceeded simultaneously over large areas if its spatial distribution is homogeneous (Bletery et al., 2016).

## 2. Model

We consider the stress field that acts upon a fault increment on a subduction megathrust. In the  $(\mathbf{x}, \mathbf{y}, \mathbf{z})$  coordinate system, where  $\mathbf{x}$  coincides with the convergence direction,  $\mathbf{y}$  is perpendicular to  $\mathbf{x}$  in the horizontal plane and  $\mathbf{z}$  points up (Figure 1), the stress tensor  $\sigma$  can be written as

$$\sigma = \begin{pmatrix} \sigma_{zz} + \Delta\sigma & \sigma_{xy} & \sigma_{xz} \\ \sigma_{xy} & \sigma_{yy} & \sigma_{yz} \\ \sigma_{xz} & \sigma_{yz} & \sigma_{zz} \end{pmatrix}, \quad (3)$$

where  $\Delta\sigma = \sigma_{xx} - \sigma_{zz}$  is a stress difference. Let  $\psi$  be the angle between the first principal component axis and the horizontal. Assuming, based on symmetry considerations, that  $\mathbf{y}$  is a principal component, the stress tensor can be rewritten as (Appendix A)

$$\sigma = \begin{pmatrix} \sigma_{zz} + \Delta\sigma & 0 & \frac{\Delta\sigma}{2} \tan 2\psi \\ 0 & \sigma_{yy} & 0 \\ \frac{\Delta\sigma}{2} \tan 2\psi & 0 & \sigma_{zz} \end{pmatrix}. \quad (4)$$

Let  $\mathbf{n}$  be a unit vector normal to the megathrust and  $\mathbf{s}$  a unit vector in the direction of the plate convergence projected onto the megathrust (Figure 1). In the  $(\mathbf{x}, \mathbf{y}, \mathbf{z})$  reference frame,  $\mathbf{n} = (-\sin \delta, 0, -\cos \delta)^T$  and  $\mathbf{s} = (\cos \delta, 0, -\sin \delta)^T$ , with  $\delta$  the apparent dip angle in the direction of the convergence (Figure 1). Based on simple geometrical considerations,  $\delta$  may be expressed as a function of the strike angle  $\phi$ , the azimuth of the convergence direction  $\lambda$ , and the actual dip angle  $\theta$  (Appendix B)

$$\delta = \arctan(\sin(\phi - \lambda) \tan \theta). \quad (5)$$

The normal and shear stress  $\sigma_n$  and  $\tau$  are then

$$\sigma_n = (\boldsymbol{\sigma} \cdot \mathbf{n}) \cdot \mathbf{n} = \sigma_{zz} + \frac{\Delta\sigma}{2}(1 - \cos 2\delta + \tan 2\psi \sin 2\delta), \quad (6)$$

$$\tau = \sqrt{(\boldsymbol{\sigma} \cdot \mathbf{n}) \cdot (\boldsymbol{\sigma} \cdot \mathbf{n}) - \sigma_n^2} = \frac{\Delta\sigma}{2}(\sin 2\delta + \tan 2\psi \cos 2\delta). \quad (7)$$

The Coulomb failure criterion gives the relationship between shear and normal stress at which the rupture initiates

$$\tau = \mu(\sigma_n - p), \quad (8)$$

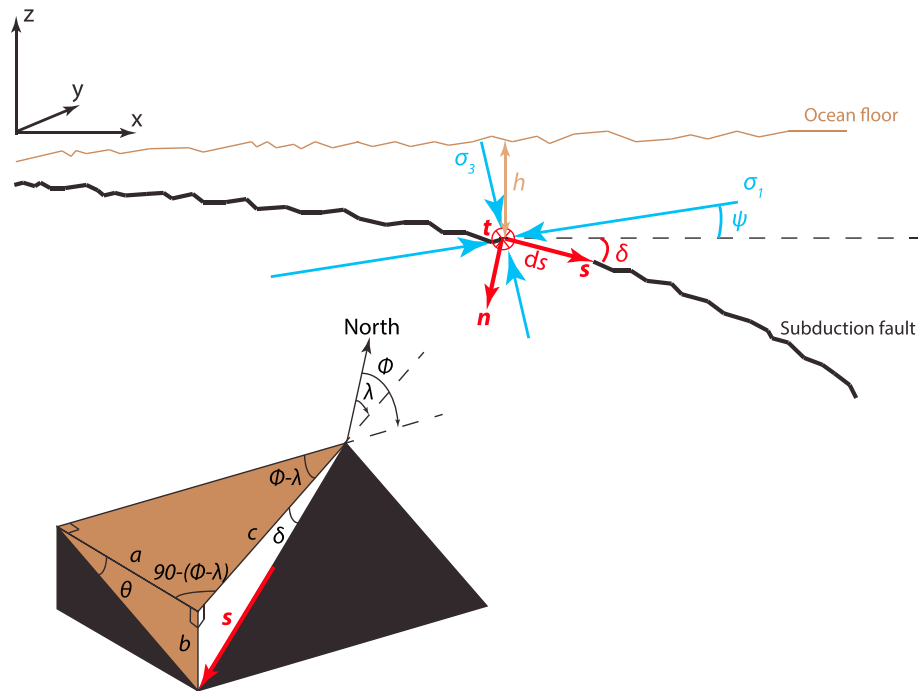


**Figure 1.** Sketch of the problem configuration. An incremental fault surface (of depth  $h$ , dip angle  $\theta$ , and strike angle  $\phi$ ) is oriented with an apparent angle  $\delta$  from the horizontal in the convergence direction of azimuth  $\lambda$ . The first principal component of the stress field  $\sigma_1$  applied to this incremental fault surface forms an angle  $\psi$  with the horizontal. Inset: relationship between the apparent dip angle  $\delta$ , the actual dip angle  $\theta$ , the strike angle  $\phi$ , and the horizontal convergence direction  $\lambda$ .

where  $\mu$  is the coefficient of friction and  $p$  is the pore fluid pressure, and we neglect cohesion for simplicity. Equations (6)–(8) enable us to express the critical stress difference required to initiate a rupture  $\Delta\sigma^c$  as a function of  $\mu$ ,  $\sigma_{zz}$ ,  $p$ ,  $\delta$ , and  $\psi$ :

$$\Delta\sigma^c = \frac{2\mu(\sigma_{zz} - p)}{\sin 2\delta - \mu(1 - \cos 2\delta) + \tan 2\psi(\cos 2\delta - \mu \sin 2\delta)}. \quad (9)$$

We can then derive from equation (7) (or equivalently equations (6) + (8)) an expression for the critical shear stress  $\tau^c$  at which a rupture initiates

$$\tau^c = \frac{\mu(\sigma_{zz} - p) \sin(2\delta + 2\psi)}{\sin(2\delta + 2\psi) + \mu(\cos(2\delta + 2\psi) - \cos 2\psi)}. \quad (10)$$

### 3. Numerical Computation

Equation (10) is quite general. The only assumptions are that the fault strength is governed by the Mohr-Coulomb failure criterion (equation (8)) and that  $\mathbf{y}$  is a principal component axis. In order to compute the distribution of shear strength, however, we need to make some stronger assumptions. A natural approximation for  $\sigma_{zz}$  is to treat it as equal to the pressure due to the mass of the upper plate; that is,  $\sigma_{zz} = \rho gh$ , with  $\rho$  the bulk density of the crust,  $g$  the acceleration of gravity, and  $h$  the depth. This case is valid as long as the gravitational loading dominates the vertical state of stress, implying that any contribution of tectonic origin to the vertical stress is negligible compared to the lithostatic pressure. A hydrostatic fluid pressure distribution could produce  $p = \rho_w gh$ , with  $\rho_w$  the bulk density of water. Although commonly assumed and useful as a starting point for exploring the controls on strength variations, the distribution of fluid pressure is relatively poorly constrained and potential deviations of  $p$  from  $\rho_w gh$  will be discussed in later sections. These two assumptions lead to

$$\tau^c = \frac{\mu(\rho - \rho_w)gh \sin(2\delta + 2\psi)}{\sin(2\delta + 2\psi) + \mu(\cos(2\delta + 2\psi) - \cos 2\psi)}, \quad (11)$$

where  $\delta = \arctan(\sin(\phi - \lambda) \tan \theta)$  (equation (5)).

We compute the distribution of shear strength using equations (11) and (5) and the Generic Mapping Tools (GMT) software. We use the distributions of dip ( $\theta$ ) and strike ( $\phi$ ) angles along the Japanese megathrusts from the SLAB1.0 model (Hayes et al., 2012), the distribution of the convergence direction  $\lambda$  given by the NNR-MORVEL56 model (Argus et al., 2011), and the distribution of the stress field orientation  $\psi$  from Hardebeck (2015). To estimate  $h$ , we use the depth of the interface given by the SLAB1.0 model (Hayes et al., 2012) corrected from the 1 arc min bathymetry given by the ETOPO1 model. Other variables are treated as constant:  $g = 9.8 \text{ m/s}^2$ ,  $\rho = 2700 \text{ kg/m}^3$ ,  $\rho_w = 1000 \text{ kg/m}^3$ , and  $\mu = 0.6$ .

Though we recognize the contribution of the preconditioned dynamic stress perturbation ( $\delta\tau$ ) and the background shear stress ( $\tau$ ) highlighted in equation (1), we proposed that the spatial variations of shear strength might be a key parameter in controlling the global distribution of mega-earthquakes because shear strength is more likely to be exceeded simultaneously over large areas if its spatial distribution is homogeneous (Bletery et al., 2016). To support this hypothesis, we further calculate the gradient of shear strength. We use the GMT software to differentiate our map of shear strength along east ( $x_E$ ) and along north ( $x_N$ ) and project the shear strength gradient in the rake-parallel ( $\frac{d\tau^c}{ds}$ ) and rake-perpendicular ( $\frac{d\tau^c}{dt}$ ) directions (with  $\mathbf{t}$  ( $= \mathbf{y}$ ) the normal to  $\mathbf{s}$  in the fault plane (Figure 1)),

$$\frac{d\tau^c}{ds} = \left( \frac{d\tau^c}{dx_E} \sin \lambda + \frac{d\tau^c}{dx_N} \cos \lambda \right) \cos \delta, \quad (12)$$

$$\frac{d\tau^c}{dt} = \frac{d\tau^c}{dx_E} \cos \lambda - \frac{d\tau^c}{dx_N} \sin \lambda. \quad (13)$$

#### 4. Results

Assuming  $\sigma_{zz} - p = (\rho - \rho_w)gh$  leads to a linear dependence of the shear strength on depth (equation (11)). This depth dependence is modified by variations in the stress field orientation with depth. Numerical computation of equation (11) using the stress field orientation of Hardebeck (2015) is shown in Figure 2. The pattern of variations in  $\tau^c$  that we determine is qualitatively consistent with the dependence of stress drop on depth observed among small earthquakes in the Tohoku rupture area (Oth, 2013; Uchide et al., 2014): higher stress drops are favored at depth where the shear stress rupture threshold is larger. It is worth noting, however, that the observed stress drops are a factor of 15 smaller than the calculated shear strengths (inset of Figure 2). A significant part of this difference could be attributed to inaccuracies in assumed pore pressures and other parameter values. For instance, assuming a coefficient of friction  $\mu$  of 0.1—such as reported by Fulton et al. (2013) in the shallow part of the Tohoku megathrust and in agreement with heat flow measurements (Gao & Wang, 2014)—instead of 0.6 reduces the difference to a factor of 2.5 (Figure S1 in the supporting information). Nevertheless, these offsets are consistent with the commonly accepted view that shear stress does not drop to zero following an earthquake; stress drops and shear strength clearly differ. In what follows, we use  $\mu = 0.6$ , but we show all equivalent figures for  $\mu = 0.1$  in the supporting information.

The distributions of the rake-parallel  $\frac{d\tau^c}{ds}$  and rake-perpendicular  $|\frac{d\tau^c}{dt}|$  components of the shear strength gradient along the Japanese megathrusts are shown in Figures 3a and 3b.  $\frac{d\tau^c}{ds}$  has a larger amplitude than  $\frac{d\tau^c}{dt}$  and is positive as long as  $\tau^c$  increases monotonically with depth (equation (11)). The norm of the shear strength gradient is dominated by the rake-parallel component, which has a higher amplitude (Figure 3c). The rake-parallel component  $\frac{d\tau^c}{ds}$  indicates particularly low gradient offshore Nankai (red patch in the south of Japan in Figure 3a). On the other hand, the rake-perpendicular component  $|\frac{d\tau^c}{dt}|$  indicates areas where the convergence direction  $\lambda$  relative to the fault orientation  $\phi$  generates heterogeneities in the shear strength distribution. Such heterogeneities seem to be minimal in the Tohoku rupture area (red patch east of the main island) and south of Nankai (Figure 3b). Even though  $|\frac{d\tau^c}{dt}|$  is of much smaller amplitude than  $\frac{d\tau^c}{ds}$ , the distributions of the two components may be of similar importance as one ( $\frac{d\tau^c}{ds}$ ) influences along-dip rupture propagation, while the other ( $|\frac{d\tau^c}{dt}|$ ) influences the lateral propagation. The amplitude of the rake-parallel and rake-perpendicular components of the shear strength gradient, as well as the norm, is reduced by a factor of  $\sim 6$  when computed with  $\mu = 0.1$  instead of  $\mu = 0.6$ , but the relative distributions are rather insensitive to the choice of  $\mu$  (Figure S2).

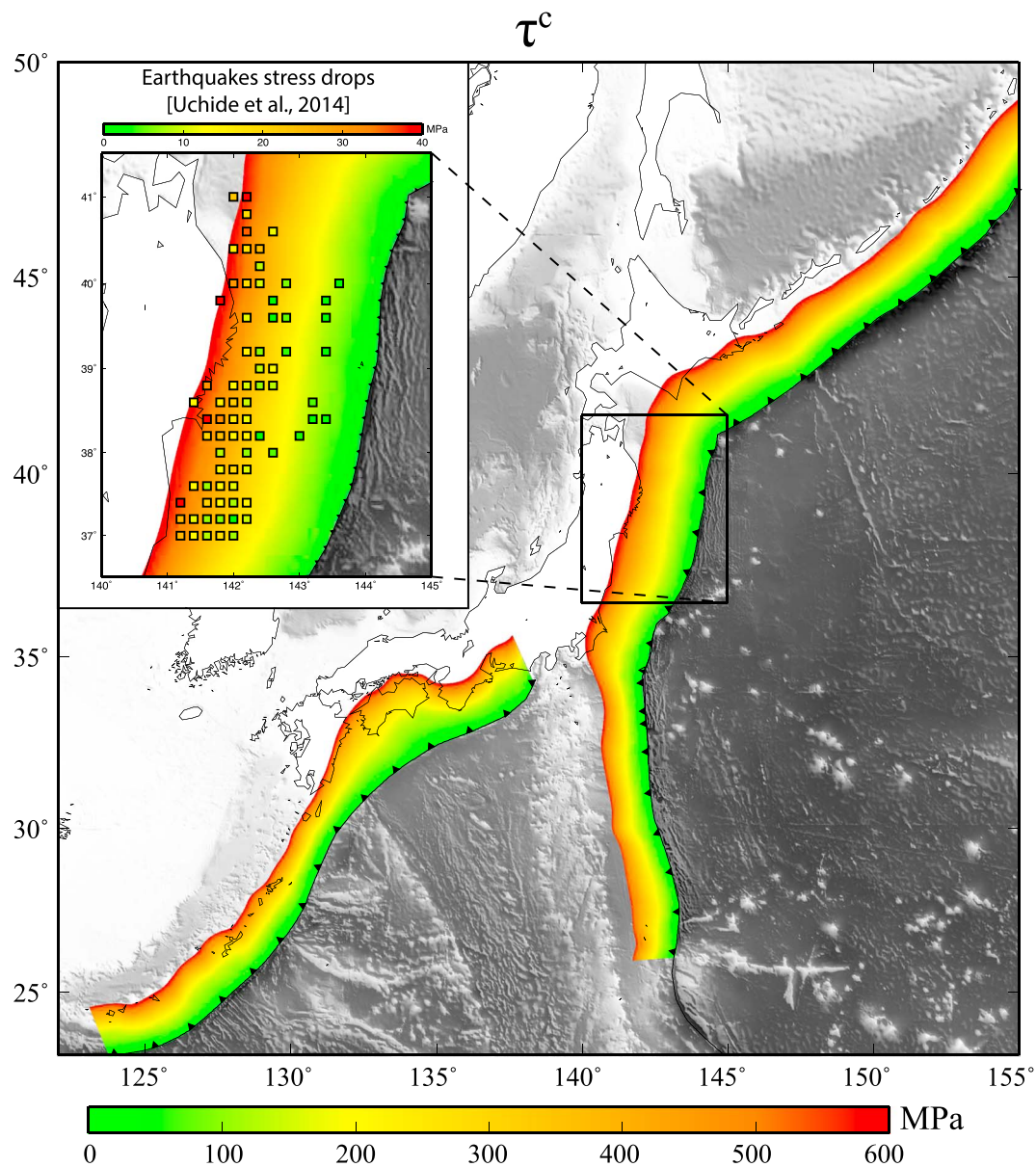


**Figure 2.** Shear strength  $\tau^c$  along the Japanese megathrusts computed from equation (11). Inset: Median stress drops (colored squares) of small earthquakes in the Tohoku-Oki area (Uchide et al., 2014) superimposed on top of the shear strength distribution.

The gradient maps are sensitive to the resolution of the different parameters in equation (11). The smaller wavelength features in Figure 3 reflect changes in the bathymetry, which is by far the best constrained parameter, with a resolution of 1 arc min. The slab1.0 model (constraining the dip and strike angles as well as the fault depth relative to sea level) has a nominal resolution of 0.5° but relies on uneven sampling in multiple data sets interpolated using Hermite splines of polynomial orders from 2 to 3, depending on depth (Hayes et al., 2012). The stress orientation is also interpolated from 0.5° wide pixels (Hardebeck, 2015). These uneven resolution limitations make our shear strength gradient maps overly sensitive to the spatial variations of the most well-resolved parameters. Though of comparable resolution, geometry dominates stress orientation effects because it varies more dramatically at the resolved scale (Figures 3a and 3c). Nevertheless, stress orientation and fault geometry may vary in different manners at much smaller scales and produce barriers at scales relevant to rupture nucleation that our long-wavelength imaging cannot capture. The rake-perpendicular component of the shear strength gradient is most sensitive to the obliquity term  $\phi - \lambda$  because

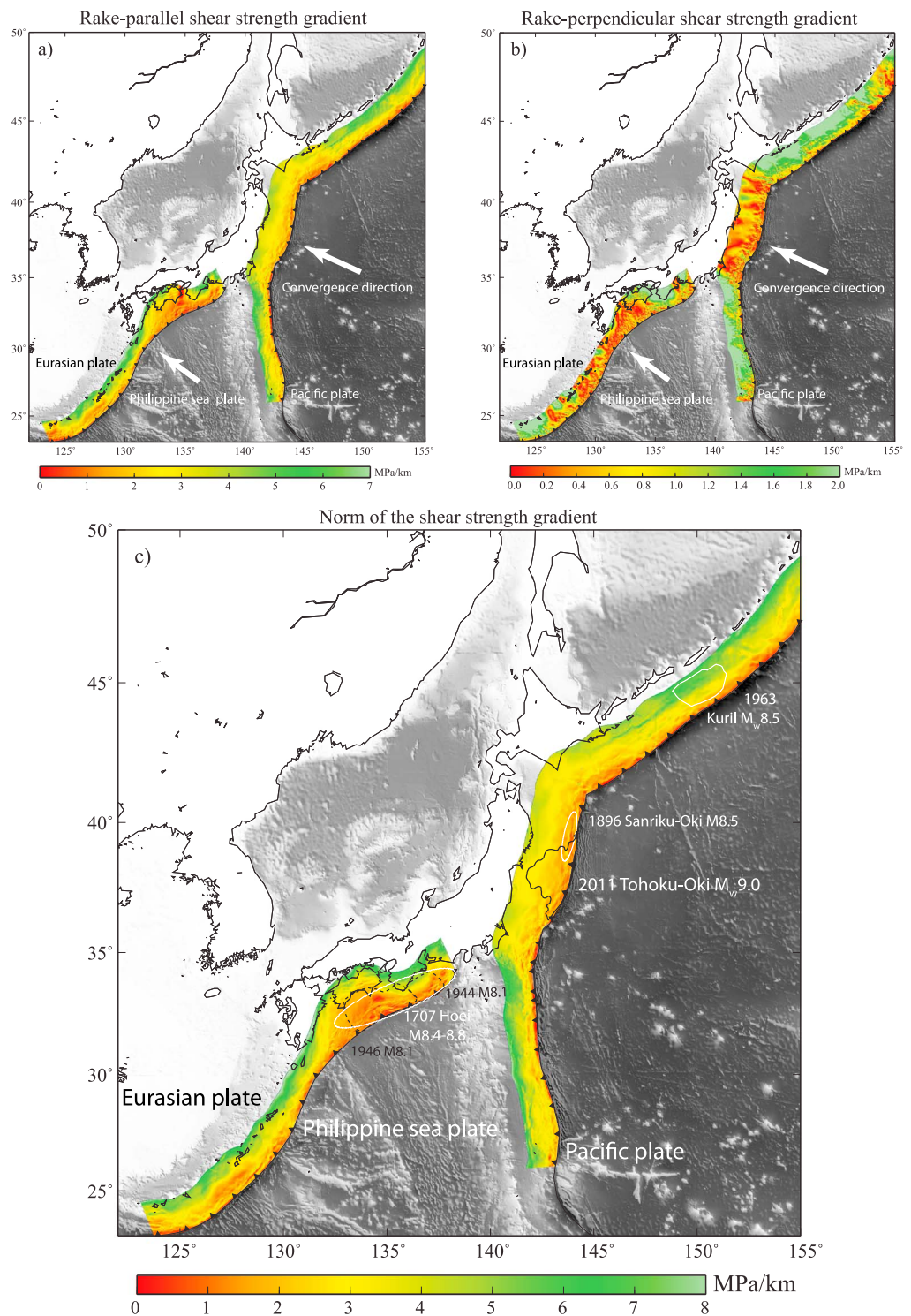


**Figure 3.** (a) Rake-parallel  $\frac{d\tau_c}{ds}$  and (b) absolute value of the rake-perpendicular  $|\frac{d\tau_c}{ds}|$  components of the shear strength gradient along the Japanese megathrusts. White arrows show the directions of plate convergences relative to the Eurasian plate. (c) Norm of the shear strength gradient. The black contour shows the location of the largest historical rupture along the Japanese megathrusts: the 2011  $M_w$  9.0 Tohoku-Oki earthquake (Bletery et al., 2014). White contours show  $M \sim 8.5$  historical earthquakes (Rhea et al., 2010; Simons et al., 2011; Furumura et al., 2011). Black dashed contours show recurrent  $M8.1-8.4$  earthquakes that ruptured simultaneously during the 1707  $M8.4-8.8$  Hoi earthquake (Furumura et al., 2011; Stein & Okal, 2007). Note that slip contours of historical earthquakes are much less well constrained than for the Tohoku-Oki earthquake.

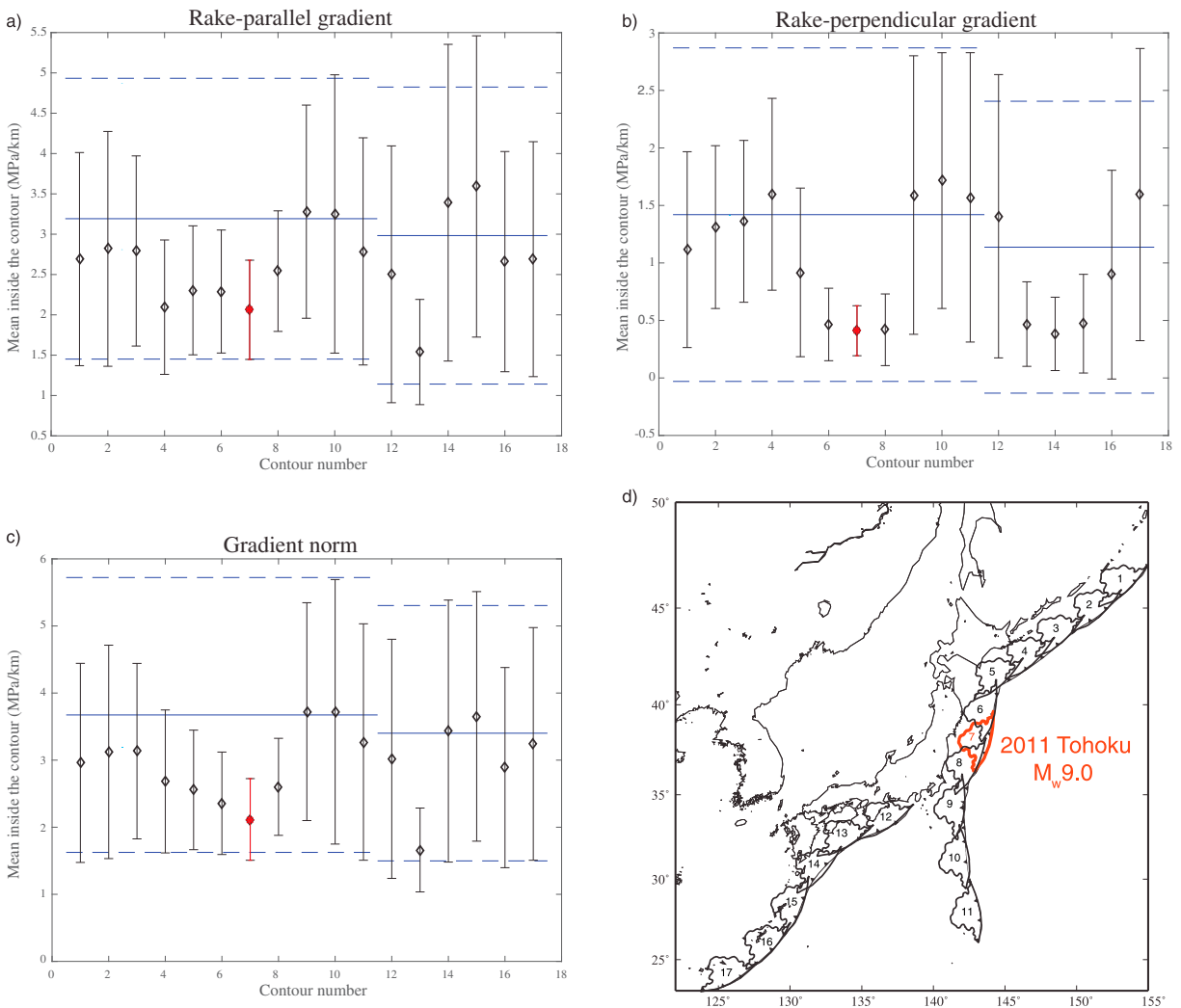


**Figure 4.** Average (black diamonds) and standard deviation (black vertical intervals) of the (a) rake parallel, (b) rake perpendicular, and (c) norm of shear strength gradient inside 17 slip contours corresponding to the (d) rupture area of the 2011 Tohoku earthquake ( $M_w$  9.0) distributed along the megathrusts. The red contour ( $n=7$ ) corresponds to the actual slip contour of the Tohoku earthquake (Bletery et al., 2014). The other 16 black contours have the same shape and area than the Tohoku earthquake but are shifted along the megathrusts. The horizontal blue solid and dashed lines show the averages and standard deviations along the seismogenic zone ( $\leq 60$  km) of the entire megathrusts.

the obliquity of the convergence makes the depth change along rake-perpendicular paths, inducing changes in strength along such paths (Figure 3b).

We proposed in an earlier paper that mega-earthquakes are favored by low shear strength gradients (Bletery et al., 2016) because homogeneous shear strength distributions facilitate synchronized failure over large fault portions. Though limited by the different parameter resolutions, Figure 3 provides material to further investigate this hypothesis. We therefore consider the slip contour of the 2011  $M_w$  9.0 Tohoku-Oki earthquake (Bletery et al., 2014), which is by far the largest rupture ever recorded in the region, and calculate the average shear strength gradient inside the rupture area (for both components and the norm). We then shift the Tohoku slip contour all along the Japanese megathrusts and compare the average shear strength gradient of Tohoku-sized areas. Our results indicate that the actual location of the Tohoku earthquake presents particularly homogeneous shear strength distributions (i.e., low shear strength gradient in all components) (Figure 4). As expected from Figure S2 relative to Figure 3, these results are insensitive to the choice of  $\mu$  (Figure S3).

Though it seems difficult to find a Tohoku-sized area of more homogeneous shear strength distribution than the actual area in which it took place, the smaller (still very large) 1963  $M_w$  8.5 Kuril earthquake seems to have ruptured a more heterogeneous fault portion (Figure 3c). Given the nature of our data sets, we are likely

insensitive to geometrical heterogeneities smaller than several tens of kilometers and frictional heterogeneities of any size, meaning that our shear strength gradient estimates essentially constitute lower bound constraints on the spatial variability of the static shear strength. In the case of the Kuril earthquake, this means that an average gradient in static shear strength of at least 4.4 MPa/km did not effectively halt a 245 km long rupture. In detail, this earthquake was actually composed of three distinct 40–60 km long subevents that ruptured successively (Beck & Ruff, 1987), consistent with a likely heterogeneous  $\tau^c$  distribution at a scale we are not able to resolve and resulting in relatively high integrated gradients at the scale to which we are sensitive (Figure 3).

The other  $M \sim 8.5$  historical earthquakes ruptured more favorable fault areas. The 1707 Hoei  $M8.4$ – $8.8$  earthquake ruptured the previously discussed red patch offshore Nankai in Figure 3a. Interestingly, this earthquake is thought to correspond to the simultaneous rupture of two patches that ruptured distinctively in 1944 and 1946 and before in 1854 (Furumura et al., 2011). The two patches seem to coincide with low shear strength gradient separated by a geometrical heterogeneity (Figure 3c).

## 5. Discussion and Conclusions

The rupture threshold  $\tau^c$  depends upon geometry ( $h, \theta, \phi$ ), rheology ( $\mu$ ), hydrology ( $p$ ), the orientation of the convergence ( $\lambda$ ), and the orientation of the stress field ( $\psi$ ), which is inherited from all the other parameters and past events (equations (10) and (5)). When the pore pressure and vertical normal stress both increase linearly with depth, the increase of  $\tau^c$  with  $h$  (equation (11) and Figure 2) suggests that larger values of  $\delta\tau$  are to be expected when an earthquake initiates at depth. Remembering that a rupture propagates as long as  $\delta\tau \geq \tau^c - \tau$  (equation (1)), it also suggests that it is much easier for a rupture to propagate in the updip direction than in the downdip direction. Indeed,  $\tau^c$ —and therefore likely  $(\tau^c - \tau)$ —decreases in the updip direction, meaning that the dynamic stress perturbation required to keep the propagation going is progressively reduced along an upwardly oriented rupture path. In special circumstances, this tendency may be counterbalanced by variations of the stress field orientation (equation (11)). However, the estimates of the stress field orientation (Hardebeck, 2015) included in our calculation of  $\tau^c$  for Japanese subduction zones do not compensate for the expected linear increase of  $\sigma_{zz} - p$  with depth (Figure 2).

The expected increase in  $\tau^c$  with depth may also be counterbalanced by nonhydrostatic distributions of pore fluid pressure. It is likely that in some areas, the distribution of pore fluid pressures is close to lithostatic (e.g., Byerlee, 1990; Faulkner & Rutter, 2001; Rice, 1992; Streit & Cox, 2001), taking the form  $p = \rho gh + C$  and breaking with the linear depth dependency of  $\tau^c$  predicted by equation (11). Near-lithostatic pore fluid pressure appears, for instance, to be required to explain the characteristics of slow earthquakes (e.g., Audet & Bürgmann, 2014; Liu & Rice, 2007; Segall et al., 2010) and other slow-slip phenomena (e.g., Bletery et al., 2017; Shelly et al., 2006), in particular their sensitivity to extremely small tidal stress perturbations (Thomas et al., 2009). Such phenomena are well documented in Nankai both at depth and in the wedge (e.g., Nakajima & Hasegawa, 2016; Obara & Kato, 2016; Shelly et al., 2006), implying that the actual shear strength in the Nankai section (contours n°12 and n°13 in Figure 4) is probably locally much smaller than suggested in Figure 4. More generally, pore pressure is expected to follow complex variations that evolve with fluid flow along the megathrust and depend upon such poorly constrained variables as the permeability of the overriding plate (e.g., Nakajima & Hasegawa, 2016; Skarbek & Rempel, 2016). In the absence of firm constraints to the contrary, the assumption of hydrostatic pore pressures should be viewed as a strong limitation of our analysis.

The present numerical computation is exploring the influence of nonfrictional parameters—nominally seafloor bathymetry, fault geometry, stress orientation, and convergence direction—on the spatial distribution of the static shear strength along the Japanese megathrusts. Though we treat  $\mu$  as constant, our approach does not require the assumption of constant friction and possible future constraints on the spatial distribution of  $\mu$  could be included in the numerical computation.  $\mu$  is also known to vary temporally as a function of the slip velocity and one or more state variables (e.g., review paper by Marone, 1998, and references therein). Although temporal variations in the friction coefficient due to rate-and-state effects are critical for our modern understanding of earthquake nucleation among other phenomena, the absolute magnitude of such changes is typically quite small ( $\leq 10\%$ ) and would be expected to have a correspondingly modest influence on our calculations of  $\tau^c$ . Dynamic weakening mechanisms, such as thermal pressurization (Lachenbruch, 1980), flash heating (Rice, 2006), or other material-dependent effects (e.g., Di Toro et al., 2011; Han et al., 2007), might

influence the evolution of shear strength more dramatically during the rupture process (e.g., Viesca & Garagash, 2015), possibly facilitating the propagation of rare large ruptures into domains that were strong enough (or rate strengthening) to withstand smaller seismic disturbances. Though beyond the scope of this study, our expression of  $\tau^c$  could be coupled with time-dependent equations governing these different mechanisms in numerical simulations of the seismic cycle and/or earthquake rupture to introduce effects of geometry, stress orientation, and convergence obliquity in these approaches. Spatial variations of the upper plate density ( $\rho$ ) could also, in future work, be included in the calculation of  $\tau^c$  (equation (11)). Bassett et al. (2016) observed a correlation between contrasts in residual density anomaly and the rupture termination of the Tohoku-Oki earthquake. They proposed that the residual density anomaly reflects changes in frictional properties. As the dependency of shear strength on density is linear (equation (11)), Bassett et al.'s (2016) observation could be reinterpreted in terms of gradients in shear strength stopping rupture propagation.

In any case, the larger shear strength at depth predicted by equation (11) is counterbalanced by larger shear strength gradient (Figures 3a and 3c). This implies that earthquakes at depth are energetic (large  $\delta\tau$ ) but spatially confined because their propagation is limited by the heterogeneity of the strength distribution. Such a mechanism would explain the high frequencies—thought to be radiated by small on-fault asperities (Madariaga, 1983)—detected at the downdip edge of the rupture of the Tohoku (Ide et al., 2011; Koper et al., 2011; Meng et al., 2011; Simons et al., 2011) and other large subduction earthquakes (Koper et al., 2012; Lay et al., 2012; Yao et al., 2013). Small-scale geometrical irregularities are themselves expected to influence rupture initiation and propagation (e.g., Dunham et al., 2011; Fang & Dunham, 2013) to the extent that such fault “bumps” are superimposed without a systematic dependence upon the large-scale geometry that we examine here. The variations in  $\tau^c$  that determine which fault segments are most prone to large earthquakes are expected to be well represented by equation (10).

The shear strength formulation we present here expresses the rupture threshold as a function of parameters for which we have some estimates along actual faults. Present estimates of stress field orientation are still rather crude, but the development of seismic instrumentation should allow for more refined studies in the future. More generally, the small-scale variations on most parameters in equations (11) and (5) (e.g.,  $h$ ,  $\theta$ ,  $\phi$ , and  $\psi$ ) are not reflected in the broad-scale estimates we used and could generate small-scale heterogeneities relevant to the nucleation and propagation of small to moderate earthquakes. Though local variations of the background shear stress are also relevant to rupture propagation (equation (1)), we showed that insights on the maximum earthquake magnitude may be deduced from the shear strength distribution alone. Though this study focused on the Japanese megathrusts, the approach may be applied to any subduction zone and the idea may be transposed to other fault systems. In particular, in the case of strike-slip faults, several studies have shown that strong variations in azimuth ( $\phi$ ) and lateral discontinuities coincide with brakes or stops in earthquake propagations (Biasi & Wesnousky, 2016; Lettis et al., 2002; Perrin et al., 2016; Wesnousky, 2006). Such variations in  $\phi$  could be interpreted as the source of large gradients in shear strength producing barriers to ruptures. Finally, we note that improved constraints on the depth dependence of pore fluid pressure and variations in the coefficient of friction may, in future work, be introduced in equation (10) to explore their influences on the distribution of shear strength along large faults.

## Appendix A: Determination of the Nondiagonal Components of the Stress Tensor

If  $\mathbf{y}$  is aligned with one of the principal components of the stress field, then the stress tensor can be expressed in the principal component reference frame as

$$\begin{pmatrix} \sigma_1 & 0 & 0 \\ 0 & \sigma_2 & 0 \\ 0 & 0 & \sigma_3 \end{pmatrix} = \begin{pmatrix} \cos \psi & 0 & \sin \psi \\ 0 & 1 & 0 \\ -\sin \psi & 0 & \cos \psi \end{pmatrix} \cdot \begin{pmatrix} \sigma_{zz} + \Delta\sigma & \sigma_{xy} & \sigma_{xz} \\ \sigma_{xy} & \sigma_{yy} & \sigma_{yz} \\ \sigma_{xz} & \sigma_{yz} & \sigma_{zz} \end{pmatrix} \cdot \begin{pmatrix} \cos \psi & 0 & -\sin \psi \\ 0 & 1 & 0 \\ \sin \psi & 0 & \cos \psi \end{pmatrix}. \quad (\text{A1})$$

The off-diagonal terms give a system of three equations that depend on  $\sigma_{xy}$ ,  $\sigma_{xz}$ , and  $\sigma_{yz}$

$$0 = \sigma_{xy} \cos \psi - \sigma_{yz} \sin \psi, \quad (\text{A2})$$

$$0 = -(\sigma_{zz} + \Delta\sigma) \sin \psi \cos \psi + \sigma_{xz} \cos^2 \psi - \sigma_{xz} \sin^2 \psi + \sigma_{zz} \cos \psi \sin \psi, \quad (\text{A3})$$

$$0 = \sigma_{xy} \sin \psi - \sigma_{yz} \cos \psi. \quad (\text{A4})$$

Solving this system gives

$$\sigma_{xy} = 0, \quad (\text{A5})$$

$$\sigma_{xz} = \frac{\Delta\sigma}{2} \tan 2\psi, \quad (\text{A6})$$

$$\sigma_{yz} = 0. \quad (\text{A7})$$

The stress tensor can then be rewritten in the  $(\mathbf{x}, \mathbf{y}, \mathbf{z})$  reference frame as equation (4).

## Appendix B: Apparent Dip Angle

Considering the inset of Figure 1, we have

$$a = c \sin(\phi - \lambda), \quad (\text{B1})$$

$$b = a \tan \theta, \quad (\text{B2})$$

$$b = c \tan \delta. \quad (\text{B3})$$

Combining (B2) and (B3) gives

$$c \tan \delta = a \tan \theta. \quad (\text{B4})$$

Using (B1), we obtain

$$\tan \delta = \sin(\phi - \lambda) \tan \theta, \quad (\text{B5})$$

from which we can derive equation (5).

### Acknowledgments

This work was supported by the National Science Foundation (NSF) project EAR-1520238. We thank Takahiko Uchide for providing his stress drop estimates shown in Figures 2 and S1 and Joan Gomberg and Nicholas M. Beeler for thoughtful comments on the manuscript. The SLAB1.0 and ETOPO1 models are available online at the following addresses [earthquake.usgs.gov/data/slab/](http://earthquake.usgs.gov/data/slab/) and [ngdc.noaa.gov/mgg/global/](http://ngdc.noaa.gov/mgg/global/), respectively. The convergence direction at the different points of the faults was calculated by the online motion calculator at this address: [geoscience.wisc.edu/~chuck/MORVEL/](http://geoscience.wisc.edu/~chuck/MORVEL/). We used the Generic Mapping Tools to compute the distributions of shear strength and their gradients ([gmt.soest.hawaii.edu/](http://gmt.soest.hawaii.edu/)).

### References

- Argus, D. F., Gordon, R. G., & DeMets, C. (2011). Geologically current motion of 56 plates relative to the no-net-rotation reference frame. *Geochemistry, Geophysics, Geosystems*, 12, Q11001. <https://doi.org/10.1029/2011GC003751>
- Audet, P., & Bürgmann, R. (2014). Possible control of subduction zone slow-earthquake periodicity by silica enrichment. *Nature*, 510(7505), 389–392.
- Bassett, D., Sandwell, D. T., Fialko, Y., & Watts, A. B. (2016). Upper-plate controls on co-seismic slip in the 2011 magnitude 9.0 Tohoku-Oki earthquake. *Nature*, 531(7592), 92–96.
- Beck, S. L., & Ruff, L. J. (1987). Rupture process of the Great 1963 Kurile Islands Earthquake Sequence: Asperity interaction and multiple event rupture. *Journal of Geophysical Research*, 92(B13), 14,123–14,138.
- Biasi, G. P., & Wesnousky, S. G. (2016). Steps and gaps in ground ruptures: Empirical bounds on rupture propagation. *Bulletin of the Seismological Society of America*, 106, 1110–1124.
- Bletery, Q., Sladen, A., Delouis, B., Vallée, M., Nocquet, J.-M., Rolland, L., & Jiang, J. (2014). A detailed source model for the  $M_w$  9.0 Tohoku-Oki earthquake reconciling geodesy, seismology, and tsunami records. *Journal of Geophysical Research: Solid Earth*, 119, 7636–7653. <https://doi.org/10.1002/2014JB011261>
- Bletery, Q., Thomas, A. M., Rempel, A. W., Karlstrom, L., Sladen, A., & De Barros, L. (2016). Mega-earthquakes rupture flat megathrusts. *Science*, 354(6315), 1027–1031.
- Bletery, Q., Thomas, A. M., Hawthorne, J. C., Skarbak, R. M., Rempel, A. W., & Krogstad, R. D. (2017). Characteristics of secondary slip fronts associated with slow earthquakes in Cascadia. *Earth and Planetary Science Letters*, 463, 212–220.
- Byerlee, J. (1990). Friction, overpressure and fault normal compression. *Geophysical Research Letters*, 17(12), 2109–2112.
- Di Toro, G., Han, R., Hirose, T., De Paola, N., Nielsen, S., Mizoguchi, K., ... Shimamoto, T. (2011). Fault lubrication during earthquakes. *Nature*, 471(7339), 494–8.
- Dieterich, J. H. (1981). Constitutive properties of faults with simulated gouge. In N. L. Carter et al. (Eds.), *Mechanical behavior of crustal rocks: The Handin volume* (Vol. 24, pp. 103–120). Washington, DC: American Geophysical Union.
- Dunham, E. M., Belanger, D., Cong, L., & Kozdon, J. E. (2011). Earthquake ruptures with strongly rate-weakening friction and off-fault plasticity. Part 2: Nonplanar faults. *Bulletin of the Seismological Society of America*, 101(5), 2308–2322.
- Fang, Z., & Dunham, E. M. (2013). Additional shear resistance from fault roughness and stress levels on geometrically complex faults. *Journal of Geophysical Research: Solid Earth*, 118, 3642–3654. <https://doi.org/10.1002/jgrb.50262>
- Faulkner, D. R., & Rutter, E. H. (2001). Can the maintenance of overpressured fluids in large strike-slip fault zones explain their apparent weakness? *Geology*, 29(6), 503–506.
- Fulton, P., Brodsky, E. E., Kano, Y., Mori, J., Chester, F., Ishikawa, T., ... Toczko, S. (2013). Low coseismic friction on the Tohoku-Oki fault determined from temperature measurements. *Science*, 342(6163), 1214–1217.
- Furumura, T., Imai, K., & Maeda, T. (2011). A revised tsunami source model for the 1707 Hoei earthquake and simulation of tsunami inundation of Ryujin Lake, Kyushu, Japan. *Journal of Geophysical Research*, 116, B02308. <https://doi.org/10.1029/2010JB007918>

- Gao, X., & Wang, K. (2014). Strength of stick-slip and creeping subduction megathrusts from heat flow observations. *Science*, *345*(6200), 1038–1041.
- Han, R., Shimamoto, T., Hirose, T., Ree, J.-H., & Ando, J.-i. (2007). Ultralow friction of carbonate faults caused by thermal decomposition. *Science*, *316*(5826), 878–881.
- Hardebeck, J. L. (2015). Stress orientations in subduction zones and the strength of subduction megathrust faults. *Science*, *349*(6253), 1213–1216.
- Hayes, G. P., Wald, D. J., & Johnson, R. L. (2012). Slab1. 0: A three-dimensional model of global subduction zone geometries. *Journal of Geophysical Research: Solid Earth*, *117*, B01302. <https://doi.org/10.1029/2011JB008524>
- Ide, S., Baltay, A., & Beroza, G. C. (2011). Shallow dynamic overshoot and energetic deep rupture in the 2011  $M_w$  9.0 Tohoku-Oki earthquake. *Science*, *332*(6036), 1426–1429.
- Koper, K. D., Hutko, A. R., Lay, T., Ammon, C. J., & Kanamori, H. (2011). Frequency-dependent rupture process of the 2011  $M_w$  9.0 Tohoku earthquake: Comparison of short-period p wave backprojection images and broadband seismic rupture models. *Earth, Planets and Space*, *63*(7), 16.
- Koper, K. D., Hutko, A. R., Lay, T., & Sufri, O. (2012). Imaging short-period seismic radiation from the 27 February 2010 Chile ( $M_w$  8.8) earthquake by back-projection of  $P$ ,  $PP$ , and  $PKIKP$  waves. *Journal of Geophysical Research: Solid Earth*, *117*, B02308. <https://doi.org/10.1029/2011JB008576>
- Lachenbruch, A. H. (1980). Frictional heating, fluid pressure, and the resistance to fault motion. *Journal of Geophysical Research*, *85*(B11), 6097–6112.
- Lay, T., Kanamori, H., Ammon, C. J., Koper, K. D., Hutko, A. R., Ye, L., ... Rushing, T. M. (2012). Depth-varying rupture properties of subduction zone megathrust faults. *Journal of Geophysical Research*, *117*, B04311. <https://doi.org/10.1029/2011JB009133>
- Lettis, W., Bachhuber, J., Witter, R., Brankman, C., Randolph, C., Barka, A., ... Kaya, A. (2002). Influence of releasing step-overs on surface fault rupture and fault segmentation: Examples from the 17 August 1999 Izmit earthquake on the North Anatolian Fault, Turkey. *Bulletin of the Seismological Society of America*, *92*(1), 19–42.
- Li, V. C., & Rice, J. R. (1983). Preseismic rupture progression and great earthquake instabilities at plate boundaries. *Journal of Geophysical Research*, *88*(B5), 4231–4246.
- Liu, Y., & Rice, J. R. (2007). Spontaneous and triggered aseismic deformation transients in a subduction fault model. *Journal of Geophysical Research*, *112*, B09404. <https://doi.org/10.1029/2007JB004930>
- Madariaga, R. (1983). High frequency radiation from dynamic earthquake. *Annales Geophysicae*, *1*, 17–23.
- Marone, C. (1998). Laboratory-derived friction laws and their application to seismic faulting. *Annual Review of Earth and Planetary Sciences*, *26*(1), 643–696.
- Meng, L., Inbal, A., & Ampuero, J.-P. (2011). A window into the complexity of the dynamic rupture of the 2011  $M_w$  9 Tohoku-Oki earthquake. *Geophysical Research Letters*, *38*, L00G07. <https://doi.org/10.1029/2011GL048118>
- Nakajima, J., & Hasegawa, A. (2016). Tremor activity inhibited by well-drained conditions above a megathrust. *Nature Communications*, *7*, 13863.
- Obara, K., & Kato, A. (2016). Connecting slow earthquakes to huge earthquakes. *Science*, *353*(6296), 253–257.
- Oth, A. (2013). On the characteristics of earthquake stress release variations in Japan. *Earth and Planetary Science Letters*, *377*, 132–141.
- Perrin, C., Manighetti, I., Ampuero, J.-P., Cappa, F., & Gaudemer, Y. (2016). Location of largest earthquake slip and fast rupture controlled by along-strike change in fault structural maturity due to fault growth. *Journal of Geophysical Research: Solid Earth*, *121*, 3666–3685. <https://doi.org/10.1002/2015JB012671>
- Rhea, S., Tarr, A. C., Hayes, G. P., Villaseñor, A., Furlong, K. P., & Benz, H. (2010). Seismicity of the Earth 1900–2007, Kuril-Kamchatka arc and vicinity: US Geological Survey.
- Rice, J. R. (1983). Constitutive relations for fault slip and earthquake instabilities. *Pure and Applied Geophysics*, *121*(3), 443–475.
- Rice, J. R. (1992). Fault stress states, pore pressure distributions, and the weakness of the San Andreas Fault. *International Geophysics*, *51*, 475–503.
- Rice, J. R. (2006). Heating and weakening of faults during earthquake slip. *Journal of Geophysical Research*, *111*, B05311. <https://doi.org/10.1029/2005JB004006>
- Segall, P., Rubin, A. M., Bradley, A. M., & Rice, J. R. (2010). Dilatant strengthening as a mechanism for slow slip events. *Journal of Geophysical Research*, *115*, B12305. <https://doi.org/10.1029/2010JB007449>
- Shelly, D. R., Beroza, G. C., Ide, S., & Nakamura, S. (2006). Low-frequency earthquakes in Shikoku, Japan, and their relationship to episodic tremor and slip. *Nature*, *442*(7099), 188–191.
- Simons, M., Minson, S. E., Sladen, A., Ortega, F., Jiang, J., ... Webb, F. H. (2011). The 2011 magnitude 9.0 Tohoku-Oki earthquake: Mosaicking the megathrust from seconds to centuries. *Science*, *332*(6036), 1421–1425.
- Skarbak, R. M., & Rempel, A. W. (2016). Dehydration-induced porosity waves and episodic tremor and slip. *Geochemistry, Geophysics, Geosystems*, *17*, 442–469. <https://doi.org/10.1002/2015GC006155>
- Stein, S., & Okal, E. A. (2007). Ultralong period seismic study of the December 2004 Indian Ocean earthquake and implications for regional tectonics and the subduction process. *Bulletin of the Seismological Society of America*, *97*(1A), S279–S295.
- Streit, J. E., & Cox, S. F. (2001). Fluid pressures at hypocenters of moderate to large earthquakes. *Journal of Geophysical Research*, *106*(B2), 2235–2243.
- Thomas, A. M., Nadeau, R. M., & Bürgmann, R. (2009). Tremor-tide correlations and near-lithostatic pore pressure on the deep San Andreas Fault. *Nature*, *462*(7276), 1048–1051.
- Uchide, T., Shearer, P. M., & Imanishi, K. (2014). Stress drop variations among small earthquakes before the 2011 Tohoku-Oki, Japan, earthquake and implications for the main shock. *Journal of Geophysical Research: Solid Earth*, *119*, 7164–7174. <https://doi.org/10.1002/2014JB010943>
- Viesca, R. C., & Garagash, D. I. (2015). Ubiquitous weakening of faults due to thermal pressurization. *Nature Geoscience*, *8*(11), 875–879.
- Wesnousky, S. G. (2006). Predicting the endpoints of earthquake ruptures. *Nature*, *444*(7117), 358–360.
- Yao, H., Shearer, P. M., & Gerstoft, P. (2013). Compressive sensing of frequency-dependent seismic radiation from subduction zone megathrust ruptures. *Proceedings of the National Academy of Sciences*, *110*(12), 4512–4517.